Energy & Environmental Science

ROYAL SOCIETY OF CHEMISTRY

PAPER

View Article Online
View Journal | View Issue

Cite this: *Energy Environ. Sci.*, 2025, **18**, 10483

Electrolytic gold plating, stripping, and ion transport dynamics through a solid-state iodide perovskite

Tuo Hu,[a] Ross A. Kerner,[b]* Aishwarya Singh,[c] Yutong Ren,[a] Ayala V. Cohen,[c] Antoine Kahn,[a] Leeor Kronik,[c] Qiangfei Xia[d] and Barry P. Rand[ae]*

The pronounced electrochemical reactivity between halide perovskites and metal electrodes can introduce mobile extrinsic metal ions which can cause device instability or enable novel functionalities. Here we systematically investigate the kinetics of gold cation (Au^+) migration in indium tin oxide (ITO)/methylammonium lead triiodide ($MAPbI_3$)/Au model devices under long-term potentiostatic biasing. Scanning electron microscopy (SEM), X-ray photoelectron spectroscopy (XPS), and density functional theory (DFT) analyses reveal that Au^+ ions, electrochemically generated at the Au anode, traverse the perovskite layer with diffusion coefficients on the order of 10^{-11} to 10^{-10} cm^2 s^{-1} and are subsequently reduced at the cathode as Au^0 clusters, resembling metal plating behavior in electrolytic cells and solid-state batteries during charging. Furthermore, reversing the applied bias strips the plated Au^0, revealing reversibility suitable for bipolar resistive switching devices and providing direct evidence of the electrochemical and ionic nature of Au transport within the perovskite matrix. Quantitatively determining diffusion coefficients and ion concentrations provides foundational inputs for future drift-diffusion modelling opportunities and allows us to relate our findings to implications on long term operation of devices like photovoltaic modules. These results clearly demonstrate the solid-state electrochemical nature of perovskite devices, highlight methods to be more quantitative about ion transport properties, provide and emphasize the importance of disentangling electro-, photo-, photoelectrochemical processes for understanding device performance and unlocking new functionalities.

Received 6th August 2025,
Accepted 17th November 2025

DOI: 10.1039/d5ee04569j

rsc.li/ees

Broader context

Halide perovskites are revolutionizing solar energy and optoelectronics with their exceptional properties. Yet, their soft lattice and mixed ionic–electronic conductivity make them vulnerable to doping and migration of extrinsic ions. Beyond causing device instability and unusual electrical responses, such ion migration can also be harnessed for functional benefits, particularly in enabling memristive and neuromorphic behavior, if controlled. Understanding the dynamics of extrinsic metal ion migration is therefore critical for either improving device stability or unlocking new perovskite-based applications. Here we explore the electrically driven migration of gold cations (Au^+) in halide perovskites. We find that Au^+ ions, electrochemically generated at the anode, migrate through the perovskite with diffusion coefficients of 10^{-11} to 10^{-10} cm^2 s^{-1} and plate at the cathode, resembling metal plating in solid-state batteries. We identify a critical pathway for Au migration to deteriorate long-term stability in photovoltaic modules. Moreover, Au migration is reversible upon reversing the bias, enabling voltage-controlled redistribution of Au and modulation of conductivity, compatible with bipolar resistive switching. This work illustrates the solid-state electrolytic nature of halide perovskites and establishes a mechanistic link between extrinsic ion transport and electrical response, revealing potential origins of anomalous electrical behavior and highlighting opportunities for developing perovskite-based neuromorphic devices.

[a] *Department of Electrical and Computer Engineering, Princeton University, Princeton, NJ 08544, USA. E-mail: brand@princeton.edu*
[b] *Chemistry and Nanoscience Center, National Renewable Energy Laboratory, Golden, CO 80401, USA. E-mail: ross.kerner@nrel.gov*
[c] *Department of Molecular Chemistry and Materials Science, Weizmann Institute of Science, Rehovoth 76100, Israel*
[d] *Department of Electrical and Computer Engineering, University of Massachusetts, Amherst, MA 01003, USA*
[e] *Andlinger Center for Energy and the Environment, Princeton University, Princeton, NJ 08544, USA*

Introduction

Metal halide perovskites have recently attracted substantial attention for a wide array of electronic and optoelectronic applications, spanning solar cells,[1–4] light emitting diodes (LEDs),[5–7] and volatile or non-volatile memristors,[8–10] owing to their exceptional electronic and optical properties. However, these materials are also known for their abundance of mobile

ionic point defects,[11–14] such as iodine vacancies (V_I^+) and iodine interstitials (I_i^+), which contribute to device instabilities and anomalous behavior, including current–voltage hysteresis[15,16] and the switchable photovoltaic effect.[17,18]

The situation becomes even more complex when perovskites interface directly with metals: their pronounced reduction/oxidation (redox) and electrochemical reactivity readily facilitates redox reactions at the perovskite/metal contact. Previous studies revealed that strongly reducing metals (*e.g.*, Al and Cr) can spontaneously induce Pb reduction and perovskite decomposition.[19] In contrast, noble metals, such as Au and Ag, are less reactive but can undergo anodic oxidation under small applied bias,[20] forming metal cations that can occupy interstitial sites within the perovskite lattice.[21] These studies clearly demonstrate that the perovskite lattice can effectively function as a solid-state electrolyte for these extrinsic metal cations, allowing rapid migration through the perovskite bulk and redistribution at device interfaces.

Injected noble metal interstitial cations, charge balanced by conduction band electrons, are stable when the Fermi level is low enough with respect to the conduction band minimum (CBM), meaning they can act as n-type dopants in perovskites.[21–23] Their formation and diffusion/migration, then, dynamically modulates carrier concentrations as a function of applied voltage and time. This redistribution of mobile extrinsic metal ions thus introduces an additional layer of operational instabilities beyond intrinsic defect effects, leading to undesirable interfaces,[24–26] perovskite decomposition,[19,27] performance degradation,[28,29] and even device failure *via* metallic shunting.[30–32] On the other hand, when precisely controlled, noble metal doping can be exploited to tune perovskite conductivity *via* voltage pulses, enabling advanced functionalities such as interface-type resistive switching memories or artificial synapses.[23,33–35] To either mitigate device instabilities or unlock novel functionalities, it is critical to develop a comprehensive understanding of both the thermodynamics of perovskite/metal electrochemical interactions and the kinetics of subsequent metal ion migration within the perovskite matrix.

In prior work, we demonstrated that electrochemical reactions occur at solid-state methylammonium lead triiodide ($MAPbI_3$)/Au interfaces at relatively low voltages ($\geq$0.8 V), during which Au is anodically oxidized and injected into the perovskite lattice *via* its interstitial sites.[20,21] In this study, we systematically investigate the kinetics and dynamics of Au migration in model devices of structure indium tin oxide (ITO, ground)/$MAPbI_3$/Au by conducting extended potentiostatic biasing experiments, followed by scanning electron microscopy (SEM) and X-ray photoelectron spectroscopy (XPS) characterization at various interfaces. We reveal that Au cations rapidly traverse the perovskite bulk until they are reduced at the cathode to Au^0 clustered islands which then propagate toward the anode, analogous to the evolution of Li dendrites in charging solid-state batteries (SSBs)[36,37] or metal dissolution-plating processes in electrorefining.[38] By integrating density functional theory (DFT) computation and semi-quantitative modelling, we provide a quantitative estimate for the diffusion coefficient (D, 10^{-11} to 10^{-10} cm^2 s^{-1}) and realistic ion concentration (C_0, 10^{15} to 10^{17} cm^{-3}) ranges for Au_i^+ in $MAPbI_3$, upon which more complex drift-diffusion modelling can be built in future work to study extrinsic metal migration kinetics in practical photovoltaic stacks under operational conditions. Finally, we demonstrate that the plated Au^0 can be partially stripped and reincorporated into the perovskite lattice by reversing the bias polarity, displaying reversible behavior compatible with bipolar resistive switching devices and offering direct evidence of the ionic transport nature of Au within the perovskite matrix. Collectively, these findings not only underscore the rapid and profound influence of Au redistribution on the electrical behavior of perovskite devices but also highlight the dual nature of perovskite devices as solid-state electrochemical cells, where metal ion migration plays a central role in both functionality and failure.

Results and discussion

Au_i^+ migration kinetics in $MAPbI_3$

As shown in Fig. 1a, the ITO/$MAPbI_3$/Au devices were first subjected to potentiostatic biasing ranging from 0.5 to 1.2 V for 2 h. The maximum applied bias was deliberately limited to 1.2 V to prevent potential MA^+ deprotonation and indium (In^{3+}) leaching at the cathode interface, which are reported to occur near this voltage threshold.[20,39] After biasing, the Au electrodes were delaminated with tape, and the perovskite layer was washed off with *N*,*N*-dimethylformamide (DMF) to expose the anodic $MAPbI_3$ top surface and the cathodic ITO interface sequentially. Subsequent characterization *via* SEM and XPS at these interfaces allow us to visualize and quantify Au accumulation resulting from the long-term biasing.

Fig. 1b shows the current density *versus* time (*J*–*t*) profiles of the devices under potentiostatic biasing at the specified voltages, with each voltage applied to a fresh pixel. The current transients exhibit non-monotonic behavior, consistent with observations from our previous study:[21] at voltages $\geq$0.8 V, the *J*–*t* curves present an initial peak, followed by a pronounced drop at intermediate times, and eventually rise to a second high plateau. In contrast, current transients at voltages below 0.7 V remain low and stable throughout the entire 2 h biasing period. Moreover, pixels biased at $\geq$0.8 V appear visibly darkened, a change that remains evident even after the perovskite layer is removed (Fig. S1b and e). Imaging of the ITO surface from one of the darkened pixels (Fig. 1c and Fig. S2, S3) reveals that the observed darkening is likely attributed to a uniform distribution of precipitated islands on the underlying ITO substrate. For comparison, SEM images of an unbiased (control) pixel are provided in Fig. S2b and c.

To identify the composition of the precipitates, we conducted XPS measurements on both the top $MAPbI_3$/Au and bottom ITO/$MAPbI_3$ interfaces (Fig. 1d, e and Fig. S4, S5). Au 4f peaks are detected at both interfaces in all darkened pixels (biased at $\geq$0.8 V), whereas devices biased below 0.8 V show no detectable changes relative to the control. As will be discussed

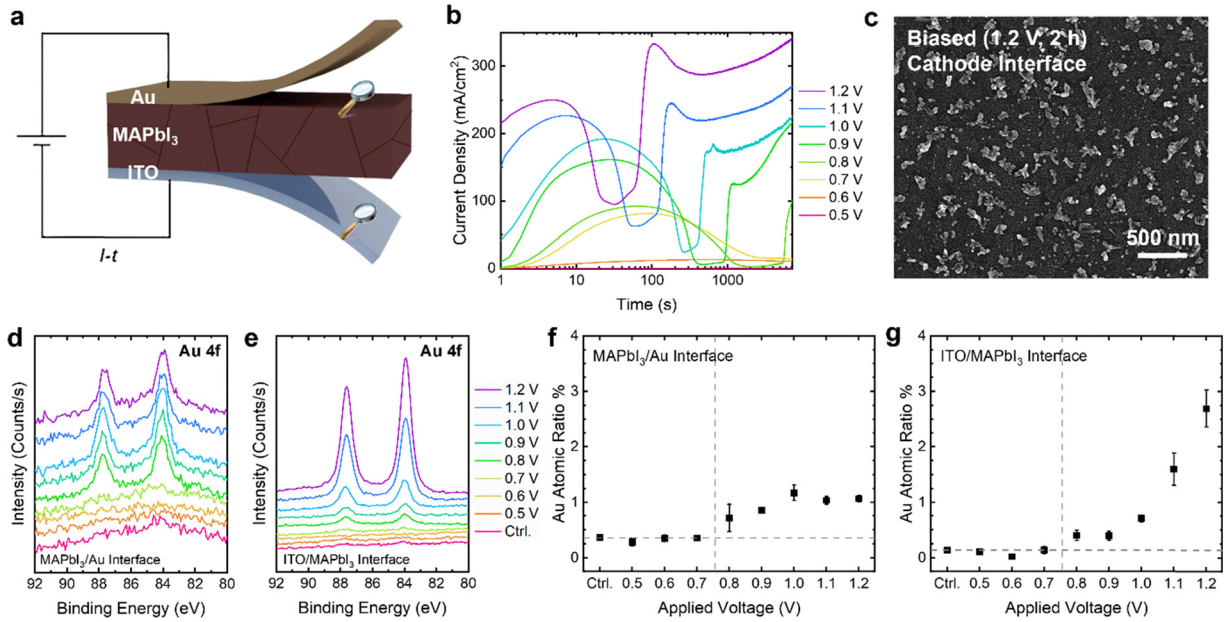

Fig. 1 Visualization and quantification of Au migration and accumulation at the anodic $MAPbI_3$/Au and cathodic ITO/$MAPbI_3$ interfaces. (a) Schematics of the device structure and characterization protocols. (b) Current density transients during 2-h potentiostatic biasing of ITO/stoichiometric $MAPbI_3$/Au devices at indicated voltages. (c) SEM image of the ITO interface after washing away the $MAPbI_3$ layer from a device biased at 1.2 V for 2 h. (d)–(g) XPS measurements of (d) and (f) the $MAPbI_3$ top surface after Au delamination and (e) and (g) the ITO interface after $MAPbI_3$ removal, following 2-h biasing at indicated voltages: (d) and (e) Au 4f spectra and (f) and (g) Au atomic percentage as a function of applied voltage. The Au atomic percentage is defined as the ratio of Au atoms to the total number of atoms detected within the XPS measurement volume. Error bars in (f) and (g) reflect the standard deviation of Au atomic percentages measured by XPS.

in detail, we believe that at voltages $\geq$0.8 V, Au from the top electrode undergoes anodic oxidation, traverses the perovskite as gold interstitial cations (Au_i^+), and is subsequently reduced and plated at the ITO cathode in the form of clustered Au^0 islands. More importantly, these results highlight the existence of a voltage threshold (V_{th}) at 0.8 V for electrochemically driven Au migration in this ITO/$MAPbI_3$/Au system, consistent with several previous studies.[20,21] Interestingly, this V_{th} for Au migration aligns with the onset ($\sim$0.8 V) of pronounced current transient features observed in Fig. 1b, implying a close link between the transients and Au migration.

As demonstrated in our previous study, a 4 $\times$ 2.5 mm^2 perovskite device (same geometry as the devices in the present study) can reach an elevated temperature of about 80 °C from Joule heating under a current density of 100 mA cm^{-2}.[40] To evaluate the potential thermal contribution, an ITO/$MAPbI_3$/Au device was thermally aged at 80 °C for two hours without applied bias. The XPS spectrum shows no detectable Au signal at the bottom ITO interface of the aged device (Fig. S6), ruling out Joule heating as the driver for gold migration across the perovskite layer on this timescale. However, it is important to note that Joule heating can greatly complicate exact determination of parameters such as activation energies and diffusion coefficients. To minimize such influence, future work on ion migration should focus on very small device areas.

As detailed in Note S1, the ionic current carried by Au_i^+ transport is estimated to account for only a negligible fraction (average transference number $\sim10^{-6}$) of the total current passed through the device over the entire biasing period. This confirms that the *J–t* features stem not from the ionic current associated with Au_i^+ transport but primarily from the rapid and significant changes to electrical properties induced by Au injection and redistribution. Moreover, it means we cannot reliably quantify ionic migration by integrating the current density.

The threshold behavior for Au migration is also clearly manifested in the plots of Au atomic % *versus* applied bias measured by XPS, as shown in Fig. 1f and g, where the Au concentrations at both interfaces show an abrupt increase above the control level at an onset of 0.8 V. Notably, the Au concentration at the bottom ITO interface increases significantly with rising bias (Fig. 1g), suggesting more extensive Au transport at higher voltages. In contrast, the Au concentration at the perovskite top surface appears to plateau around 1 atomic% under elevated biases ($\geq$1.0 V) (Fig. 1f). This saturation may hint to formation of a thin, self-limiting passivation layer at the $MAPbI_3$/Au interface that contains Au at this specific concentration, reminiscent of a cathode–electrolyte interphase (CEI) commonly observed in SSBs.

We performed the same set of measurements on devices with super-stoichiometric (10% methylammonium iodide (MAI)-excess) and sub-stoichiometric (10% MAI-deficient) $MAPbI_3$ as well to examine how perovskite stoichiometry affects the thermodynamics and kinetics of Au migration in this system. Fig. S7a and c show the *J–t* curves of the MAI-excess and MAI-deficient devices under various applied voltages

respectively. While the MAI-excess device shows a slightly more suppressed initial current peak, the non-stoichiometric devices overall exhibit current transients that qualitatively resemble those of the stoichiometric device, all following the characteristic "peak-trough-plateau" profile with the same onset voltage (~0.8 V). Significant, too, is that the non-stoichiometric devices show an identical voltage threshold for Au migration and accumulation at the ITO interface as the stoichiometric device (0.8 V), as evidenced by the XPS results in Fig. S5 and S8. These results suggest that perovskite stoichiometry does not affect Au oxidation thermodynamically.

On the other hand, XPS results (Fig. S8d–f) reveal that the amount of Au plated at the ITO increases with decreasing MAI concentration. This trend is also visually evident, as the MAI-deficient devices exhibit significantly darker pixels compared to the MAI-excess ones (Fig. S1). Meanwhile, it appears that the timing of the *J*–*t* features shifts earlier in time as the MAI concentration decreases (Fig. S7). All these findings imply that Au may migrate faster in a MAI-deficient environment, indicating that perovskite stoichiometry or initial defect properties can alter the kinetics of Au transport. The higher concentrations of various defects in the MAI-deficient samples likely impose less hindrance for Au_i^+ migration through the perovskite lattice, leading to the observed more rapid Au transport. Additionally, given the comparable grain size, alignment, and film thickness across all three compositions (Fig. S9), the observed stoichiometry-dependent transport kinetics further implies that Au migration is not limited to grain boundaries. Most importantly, a previous study showed Au^0 aggregating at the ITO/SnO_x cathode within the grain interiors and not at grain boundaries.[41] This must proceed predominantly through the perovskite bulk, where mobile Au_i^+ is thermodynamically most stable,[21] supporting our conclusions.

The identical voltage threshold for both the prominent current transient features in potentiostatic biasing and Au accumulation at the ITO interface suggests close correlation between the *J*–*t* characteristics and Au migration through the perovskite layer. Thus, we examine how the Au accumulation profile evolves over the course of the biasing period. As exemplified in Fig. 2a, a typical current transient can be characterized by four distinct time points on the *J*–*t* curve: *T*1 marks the time when the current reaches its initial peak; *T*2 corresponds to the lowest point of the subsequent trough; *T*3 denotes the end of the sharp current rise following the trough; and *T*4 represents the conclusion of the 2 h biasing period.

To explore this further, we applied a 1.1 V bias to different ITO/stoichiometric $MAPbI_3$/Au pixels until each of the *T*1–*T*4 time points respectively, followed by XPS and SEM analyses on both the top $MAPbI_3$ surface and the ITO interface at each corresponding time point. As shown in the XPS data collected at the bottom ITO interface (Fig. S10b), Au 4f peaks first appear at *T*2, marking the onset of detectable Au precipitation at the

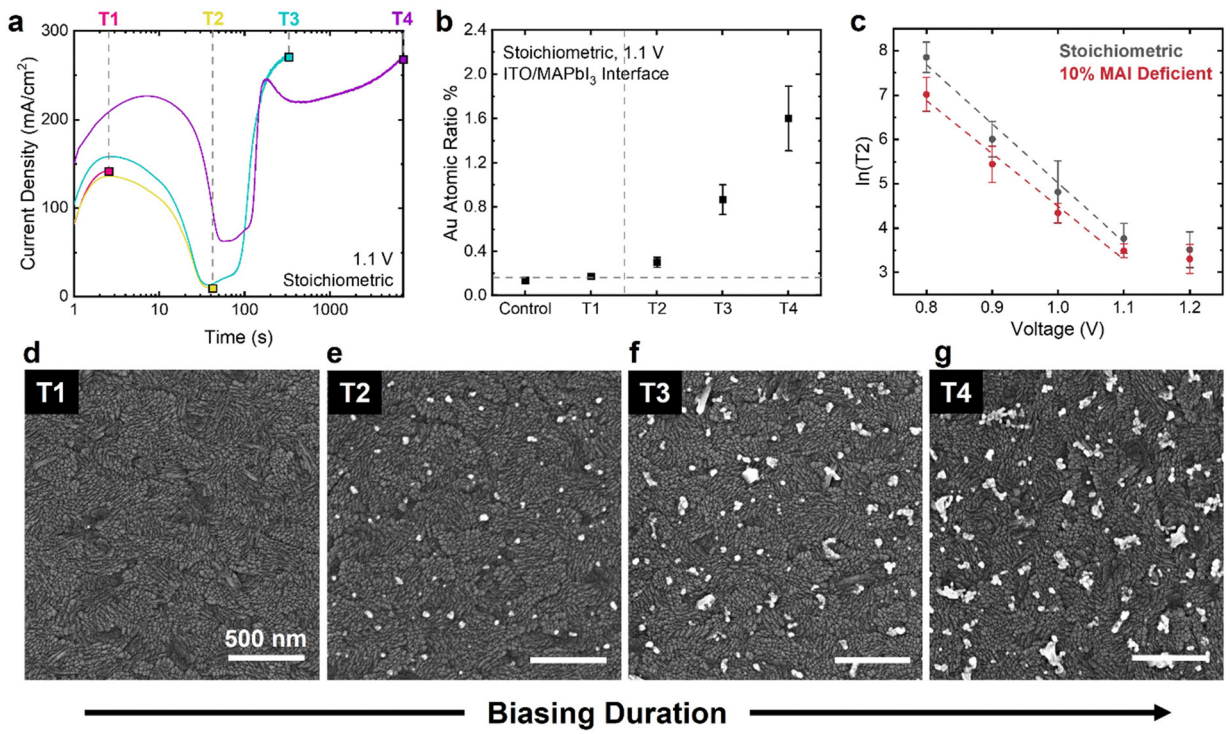

Fig. 2 Correlation between *J*–*t* transients and Au migration kinetics. (a) Illustration of the four characteristic time points (*T*1–*T*4) on the *J*–*t* curves exemplified using data collected from ITO/stoichiometric $MAPbI_3$/Au devices biased at 1.1 V. (b) Au atomic percentage at the ITO interface determined *via* XPS measurements at each time point. (c) Natural logarithm of *T*2 values for stoichiometric and 10% MAI-deficient devices as a function of applied voltage. Linear fits are included to highlight their linear relationship. (d)–(g) SEM images of the ITO interface after $MAPbI_3$ removal at each corresponding biasing time point. Error bars in (b) reflect the standard deviation of Au atomic percentages measured by XPS. Error bars in (c) reflect the standard deviation of *T*2 values extrapolated from the corresponding *J*–*t* curves.

cathode. From this point onward, the Au atomic percentage exceeds the control level and continues to increase over time (Fig. 2b). This trend is further corroborated by SEM imaging of the ITO interface (Fig. 2d–g): while the surface at $T1$ resembles that of an unbiased pixel, Au islands begin to appear at $T2$, progressively growing in size and covering a larger portion of the image area as biasing continues. However, no Au 4f signals are observed at the $MAPbI_3$ top surface until $T4$ (Fig. S11a and b), indicating that Au accumulation at the anodic interface occurs much later in time. This delayed Au appearance suggests that Au^0 may accumulate in the perovskite layer progressively from the cathode toward the anode. Nevertheless, for MAI-excess devices, after taking account for the series resistance of ITO, the actual voltage across the perovskite layer falls below the 0.8 V threshold during the later stages of biasing for all applied voltages (Fig. S12). This subthreshold voltage in MAI-excess devices effectively halts further Au_i^+ injection, which explains the absence of detectable Au signal at the $MAPbI_3$/Au interface even after 2 hours of biasing (Fig. S8a).

Similar J–t characteristics and an identical temporal onset ($T2$) of Au accumulation at the ITO interface are consistently observed when we extend the testing protocols to devices with different stoichiometries (stoichiometric *versus* MAI-deficient) under different applied voltages (0.9 V and 1.1 V) (Fig. S10, S13 and S14). This consistency suggests that $T2$ represents the characteristic time required for Au to traverse the perovskite layer, rendering it a useful benchmark for assessing Au migration kinetics in perovskites. Note that MAI-excess devices are excluded from this analysis due to their less clearly defined current features relative to the other two compositions. Based on this analysis, we systematically applied bias to devices with either stoichiometric or MAI-deficient $MAPbI_3$ layers across a voltage range of 0.8–1.2 V (Fig. S15 and S16). At least 3 pixels were tested for each condition to ensure statistical relevance. This allows us to construct a distribution of $T2$ as a function of applied voltage for both stoichiometries, as illustrated in Fig. 2c and Fig. S17. For a fair comparison, the thicknesses of the perovskite films with different stoichiometries are controlled to be consistent at approximately 260 nm (Fig. S9). When the device is biased at the threshold voltage (0.8 V), nearly all the applied voltage is expected to drop at the $MAPbI_3$/Au interface, enabling the electrochemical reaction while leaving the voltage drop across the perovskite bulk negligible. Under this condition, Au_i^+ migration is primarily driven by diffusion. Hence, we can use the $T2$ values at 0.8 V, along with density functional theory (DFT) computation and diffusion-based modelling, to quantitatively estimate both the diffusion coefficient of Au_i^+ in $MAPbI_3$ and the Au_i^+ doping concentration at the anode interface (C_0).

Specifically, as detailed in Note S2, we started with DFT simulations to model the Au_i^+ migration pathway within a $MAPbI_3$ unit cell using the nudged elastic band (NEB) method, finding an activation energy (E_A) of 0.46 eV (Fig. S17). This value agrees very well with the value of 0.42 eV reported by Ming *et al.*,[42] even though more stringent convergence parameters were used in this work (see Methods in the SI). Because the diffusion coefficient depends exponentially on the migration barrier height, we assume a reasonable uncertainty of ± 0.05 eV in the computed value. This then leads to a diffusion coefficient (D) in the range of 1.8×10^{-11} to 8.8×10^{-10} $cm^2\ s^{-1}$. With these DFT-derived diffusion coefficients, we can estimate the Au_i^+ doping concentration at the anode interface using the temporal onset of Au plating on ITO ($T2$) combined with modeling based on the assumption of purely diffusive transport and focusing the analysis at the threshold voltage 0.8 V to minimize the possibility of significant electric fields. This results in a C_0 range of 1.3×10^{15} to 1.4×10^{17} cm^{-3}, which is consistent with the typical defect densities reported for polycrystalline perovskites (10^{15}–10^{17} cm^{-3}),[43–45] validating the credibility and practicality of our experimental methodology and the diffusion-based model. Furthermore, compared to the broad spectrum of reported ionic defect diffusivities in $MAPbI_3$ (*e.g.*, 10^{-12} to 10^{-6} $cm^2\ s^{-1}$ for V_I^+, 10^{-11} to 10^{-8} $cm^2\ s^{-1}$ for I_i^-, and 10^{-16} to 10^{-12} $cm^2\ s^{-1}$ for MA^+),[46–51] our estimated Au_i^+ diffusion coefficients (10^{-11} to 10^{-10} $cm^2\ s^{-1}$) lie on the lower end of these. Even with the limitations of our model (as discussed in Note S2) in mind, the above method exemplifies a straightforward approach to quantitatively investigating the kinetics of extrinsic metal ion migration in halide perovskites which may also be applicable to other metals, such as Ag or Cu, in various perovskite compositions. Most importantly, we have combined theory and experimental data to provide the quantities E_A, D, and realistic ranges for C_0 that can be used in future studies and incorporated into drift-diffusion models for further evaluation.

Our D and C_0 are estimated at relatively low values, yet we still observe Au_i^+ diffusion affecting device behavior on timescales as short as 40 s at 1.1 V. Diffusion is not sufficient to explain the kinetics of the Au_i^+ migration under such conditions. Under suprathreshold biasing conditions, we observe an empirical linear correlation between the natural logarithm of average $T2$ values and the applied voltage (Fig. 2c), a trend that cannot be fully explained by diffusion or drift alone. As discussed in Note S2, both the stronger electric field-induced drift and the increased C_0 at higher voltages likely contribute to the much faster Au_i^+ transport under suprathreshold biasing conditions. Although a complete understanding of the empirical trend seen in Fig. 2c remains challenging, it clearly reflects the complex interplay between drift and diffusion in ion transport within perovskites. Furthermore, the results show that slightly surpassing the threshold voltage by just 0.3 V can reduce the Au migration time across the perovskite by nearly two orders of magnitude (from $\sim$2700 s to 45 s). This demonstrates that even a modest increase beyond the electrochemically stable voltage range can drastically accelerate ion migration, underscoring the need to accurately identify electrochemical stability windows for different perovskite/metal interfaces. Lastly, we observe that Au migration occurs over a shorter timescale in MAI-deficient devices than in stoichiometric ones at every applied voltage, further confirming the faster Au transport kinetics in an MAI-deficient environment.

Reversible Au plating/stripping for novel functionalities

We further demonstrate the electrochemical nature of Au migration within the perovskite by showing that Au^0 plated at the ITO can be stripped and reincorporated into the perovskite by reversing the bias polarity. To this end, four ITO/stoichiometric $MAPbI_3$/Au pixels from the same substrate were subjected to different biasing conditions. The first pixel, termed the "plated-only" device, was biased at 1 V until the current transient reached *T*3, when substantial Au^0 plating is expected at the ITO interface. As a comparison, the second pixel underwent the same plating protocol as the first, immediately followed by a stripping process involving a −1 V bias at the Au electrode for 2 h. It is thus referred to as the "stripped" device. To ensure that a negative bias at the Au electrode alone would not induce Au redistribution, the third pixel, called the "reverse-only" device, was biased at −1 V for 2 h. Finally, the fourth pixel served as the "control" and was left unbiased to provide a reference. After biasing, we peeled off the top Au electrode and washed off the perovskite layer to expose the ITO interface for XPS and SEM measurements.

Fig. 3a presents the current transients of the first three devices. Note that the current in the "reverse-only" device stays stable and low throughout the 2 h biasing period, suggesting the relative electrochemical stability of the Au electrode at this negative bias (note, we anticipate some reactions at −1.2 V and possibly −1.1 V).[20,39] This is expected since Au electrodes can only be oxidized under anodic conditions, and they are well-known to be inert and stable under a cathodic bias (the inverse is true for ITO).[30] More importantly, the *J*–*t* characteristics during the stripping process (blue curve in Fig. 3a) qualitatively resemble the early stages of the plating processes (red and yellow curves in Fig. 3a), which is more visually apparent when the absolute values of the current densities are plotted together in Fig. S19e. This similarity suggests that the plated Au^0 at the ITO can function as an Au anode when the voltage polarity is reversed and impose a similar effect to the perovskite film as before. The only difference is that the stripping process does not display the final current increase seen in plating, as the anode during stripping does not have a large reservoir of Au, preventing further doping at long times when available Au is exhausted. A detailed comparison of current transient features between plating and stripping can be found in Note S3.

According to the XPS results in Fig. 3b and c, the Au 4f peak intensity and the corresponding Au atomic percentage at the stripped ITO interface are substantially lower than those of the plated sample. This indicates that many of the plated Au^0 islands are re-oxidized into Au_i^+ cations and reincorporated

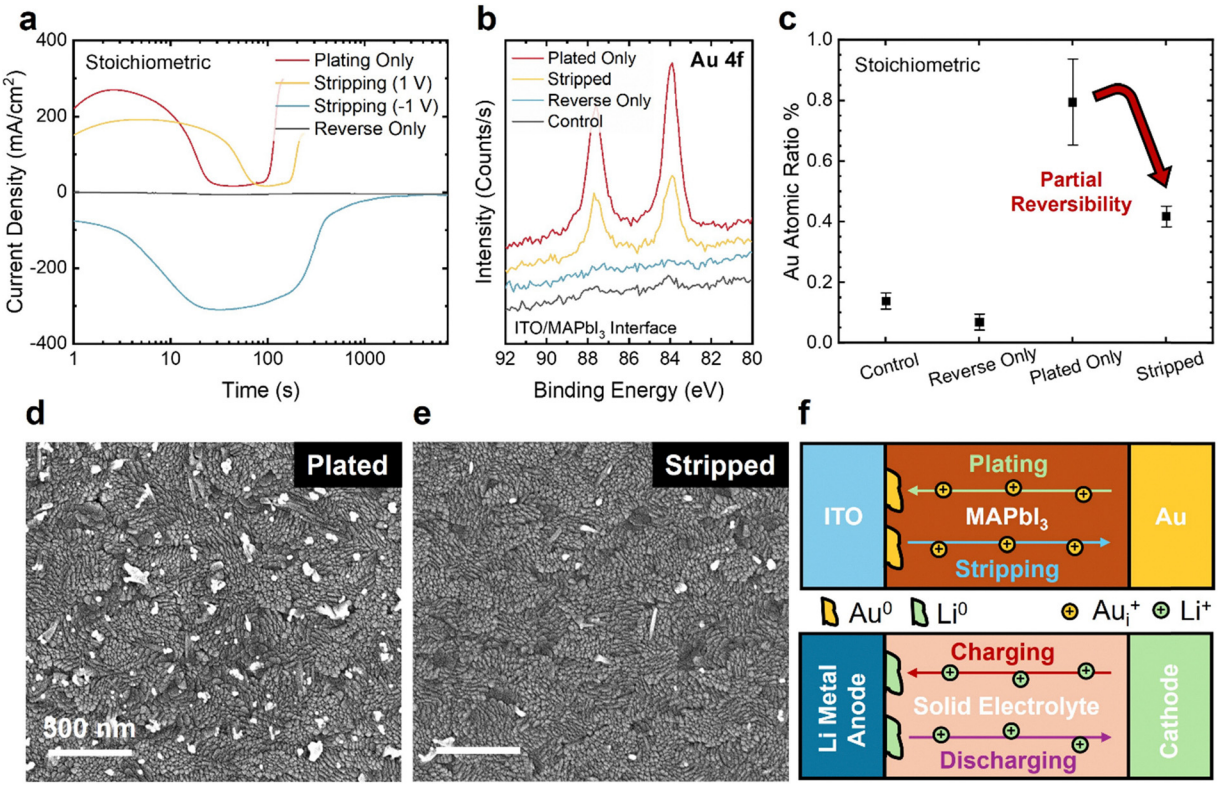

Fig. 3 Partial reversibility of Au migration in ITO/$MAPbI_3$/Au devices. (a) *J*–*t* characteristics during the Au plating process for the "plated-only" device (1 V, *T*3, red), as well as for the "stripped" device during plating (1 V, *T*3, yellow) and subsequent stripping (−1 V, 2 h, blue). A "reverse-only" device (−1 V, 2 h, gray) is included to show the stability of Au as a cathode. (b) and (c) XPS analysis at the ITO interface after perovskite removal: (b) Au 4f spectra and (c) Au atomic percentages for each biasing condition. (d) and (e) SEM images of accumulated Au^0 at the ITO interface for the (d) "plated-only" and (e) "stripped" pixels. (f) Schematic comparison between our ITO/$MAPbI_3$/Au device and a prototypical solid-state battery, highlighting the conceptual similarity between the two. Error bars in (c) reflect the standard deviation of Au atomic percentages measured by XPS.

into the perovskite lattice upon stripping, leaving behind only residual Au^0 likely due to poor interfacial contact with the perovskite or inadequate electrical connection to the ITO, analogous to electrically isolated, ''dead'' Li that limits ideal reversibility in SSBs.[52] This trend is visualized through SEM imaging of the plated-only (Fig. 3d) and the stripped (Fig. 3e) pixels, where both the density and size of the accumulated Au^0 islands are notably reduced after stripping, consistent with XPS results. Furthermore, similar results are observed in non-stoichiometric samples as well: both MAI-excess and MAI-deficient devices exhibit qualitatively similar current transient characteristics between plating and stripping processes (Fig. S19), along with a substantial reduction in the Au 4f XPS signal at the ITO interface following stripping (Fig. S20). These results collectively demonstrate the partial reversibility of Au migration and accumulation in the perovskite film, irrespective of its stoichiometry.

These findings not only reinforce the highly mobile nature of Au species within perovskite films but also draw a compelling analogy between the observed electrochemical plating of Au at the ITO interface and the electrolytic deposition of Li metal on the anode during charging in SSBs. As illustrated in Fig. 3f, a prototypical SSB consists of three major layers: a lithium-conducting but electrically insulating solid electrolyte layer is sandwiched between a cathode and an anode. During charging, the Li^+ ions diffuse out of the cathode (typically a metal oxide) and migrate through the electrolyte to the anode (typically lithium metal or graphite) where Li^+ ions are electrolytically reduced and plated as metallic Li^0.[53,54] Analogously, in our ITO/$MAPbI_3$/Au devices, the iodide framework in the $MAPbI_3$ crystal structure allows high densities of interstitial sites through which monovalent cations can migrate.[40] As a result, the perovskite effectively functions as a solid electrolyte, allowing Au cations to migrate toward the ITO cathode where they are reduced and deposited as Au^0 clusters. In contrast to discharging in SSBs – where the plated Li metal at the anode is spontaneously oxidized back into Li^+ ions that diffuse towards the cathode while the stripped electrons flow through the external circuit to do electrical work[53,54] – Au stripping in our system is an electrolytic process that requires an applied bias to drive the re-oxidation of Au^0 back to Au^+ (Au is not spontaneously stripped from a plated device after resting at short circuit overnight (Fig. S21)). Despite this difference, the observed reversibility of Au plating and stripping confirms the ionic transport nature of Au within the perovskite electrolyte, akin to Li^+ transport in SSBs.

Furthermore, the electrolytic nature of halide perovskites opens opportunities for new device functionalities. For example, other coinage metals such as Ag or Cu may also undergo similar ionic transport and plating behavior through the perovskite matrix. Thus, upon further device optimization, including cathode material selection, perovskite composition modulation, and interfacial engineering, halide perovskites could potentially be utilized as solid-state electrolytes for applications resembling electroplating or electrorefining of various metals. In addition, we demonstrate that applying biases of opposite polarities enables controlled tuning of device conductivity through the reversible redistribution of Au species within the perovskite film. This suggests that extrinsic metal doping and interfacial plating/stripping can be potentially exploited for achieving bipolar resistive switching in perovskite-based memristors or neuromorphic devices, where resistance states are controllably and reversibly switched by applied biases.

Mechanistic interpretation of Au_i^+ doping effects on device electrical properties

Lastly, we propose to rationalize the evolution of the *J–t* transients during potentiostatic biasing (*e.g.*, Fig. 2a) as a synergistic outcome of n-doping by injected Au_i^+ and interfacial modification due to Au species redistribution. The microscopic processes within the device – including the oxidation, migration, and re-deposition of Au species, along with the corresponding changes in the energetic band structure – are illustrated in Fig. 4.

To begin with, we assume the as-fabricated perovskite bulk to be weakly p-type as demonstrated in our previous work using a similar device structure.[21] At early times of biasing, the current uptake is attributed to near-interface-limited ion motion near the anode happening over a timescale of seconds. For example, underpotential deposition (UPD) reactions can occur at the $MAPbI_3$/Au interfaces where iodide anions (I^-) from $MAPbI_3$ are oxidized and adsorbed onto the Au surface as I^0_{UPD} (Fig. 4e).[27] This iodine adsorption significantly increases the Au work function (Fig. 4i red arrows),[55] enhancing efficient hole injection at the $MAPbI_3$/Au interface and contributing to the initial rise in current density prior to *T*1 (Fig. 4a). At intermediate timescales, upon application of a suprathreshold bias, Au is anodically oxidized to Au_i^+ cations which enter the perovskite film at the $MAPbI_3$/Au interface (Fig. 4f). These injected Au_i^+ cations act as n-type dopants, which compensate for the background hole concentration (Fig. 4j, gray dashed lines), leading to a significant drop in current between *T*1 and *T*2 (Fig. 4b). Meanwhile, as the perovskite gradually transitions from p-type to nearly intrinsic, the Fermi level shifts upwards and increases the built-in potential barrier of the $MAPbI_3$/Au Schottky junction (Fig. 4j, red arrows). This enlarged potential barrier further suppresses carrier transport, consistent with the low current level observed at *T*2.

As Au^0 clusters begin to accumulate at the ITO interface from *T*2 onward, it indicates that a considerable number of Au_i^+ ions have already traversed the perovskite bulk and reached the cathode. With Au_i^+ dopants distributed throughout the perovskite bulk, the material is effectively converted to n-type. Concurrently, the rising concentration of Au_i^+ dopants near both electrodes narrows the depletion width of the Schottky junctions (Fig. 4k, red arrows), promoting efficient electron injection *via* tunneling. Together, the bulk doping and the modifications in interfacial energy barriers at both contacts shift the dominant charge carriers from holes to electrons and drive the sudden current increase observed after *T*2 (Fig. 4c). While the dominant carrier type changes, their transport direction reverses too, so the overall current flow direction remains. As biasing continues,

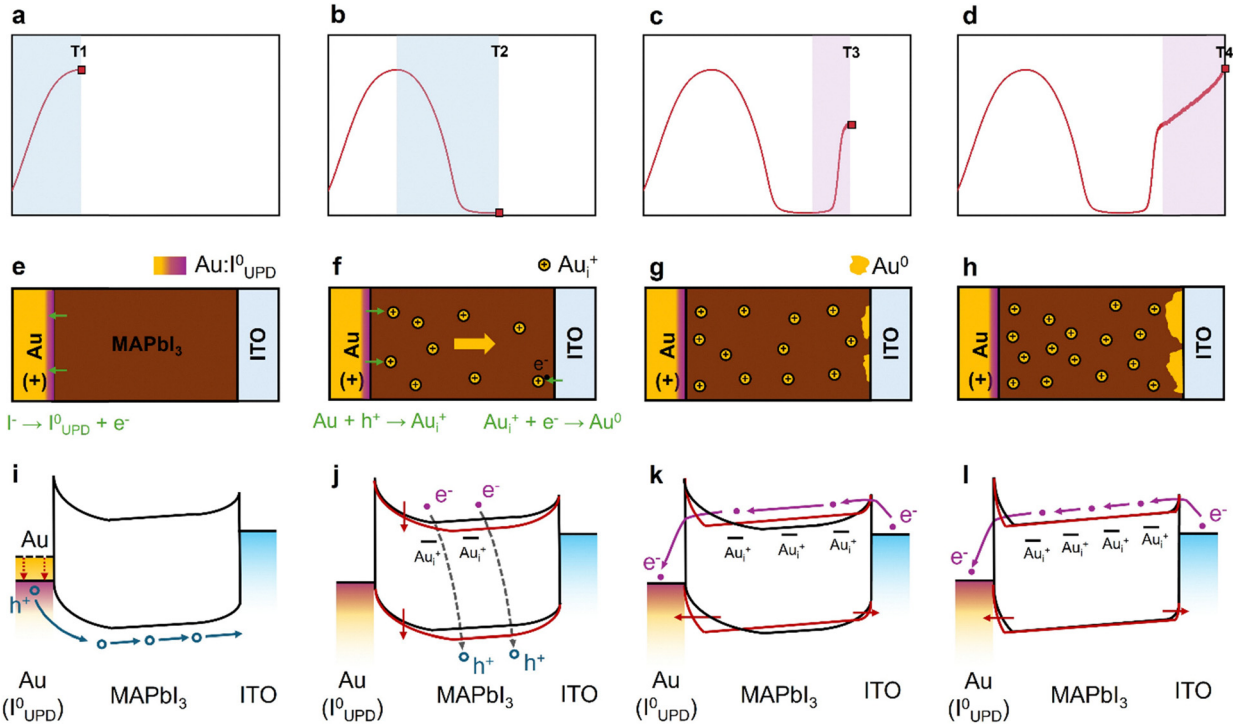

Fig. 4 Proposed model illustrating the synergistic influence of Au_i^+ electrochemical doping and Au redistribution in explaining the current transient features during potentiostatic biasing. Each column corresponds to one of the four biasing stages defined by the characteristic time points ($T1$–$T4$). (a)–(d) Representative current *versus* time transients highlighting each characteristic time point and conduction stages between them, with the blue shading representing hole conduction and the purple shading representing electron-dominated conduction. (e)–(h) Schematics depicting Au migration and accumulation at each stage. (i)–(l) Corresponding qualitative device energy diagrams. Black and red colors are used to reflect changes of the band structure, showing its evolution from the initial black to the new red configuration for a given time period, as also hinted by the solid red arrows. The dashed red arrows in (i) reflect a spontaneous shift that may occur prior to biasing ($t < 0$).

ongoing Au_i^+ doping raises the electron density (Fig. 4l), leading to the gradual current increase seen at the later stage of biasing (Fig. 4d). This model suggests that the initial current peak is dominated by holes while the later current plateau is mainly governed by electrons, consistent with the mechanism proposed in our previous study.[21] A proposed mechanistic interpretation of the stripping current transient features is presented in Note S3.

Broader outlook and its implications for photovoltaics

Overall, the above findings highlight the unexpectedly rapid kinetics of Au migration within perovskites, capable of traversing a 260 nm perovskite layer within ~40 s under a modest voltage of 1.1 V, and its pronounced impact on the electrical properties of these materials. Clearly, small changes to the Au defect concentrations near the Au electrode have a significant effect on device characteristics on the timescale of 1–2 s as well. This underscores the need for careful consideration of Au migration and redistribution when analyzing data from space-charge-limited current (SCLC), field-effect transistor (FET), or Hall effect measurements involving direct perovskite/Au contacts, where prolonged measurements at elevated voltages should be ideally avoided. Meanwhile, further investigations into the dynamics of Au transport and accumulation within the perovskite bulk, under device-operating conditions, may provide valuable insights into the origins of performance instabilities and anomalies such as hysteresis or the switchable photovoltaic effect.

The most significant potential application of halide perovskites at the moment is photovoltaic (PV) modules, and our results can offer new outlooks on impacts from electrode reactions affecting this technology. A solar cell is under illumination in addition to under voltage bias. Thus, one must disentangle electrochemical, photochemical, and photoelectrochemical processes.[14] Specifically, direct perovskite/Au contact is more common in practical perovskite solar cells and modules than often assumed. First, no thin film is entirely free of defects, and Au migration can readily occur through localized regions of direct perovskite/Au contact at defects such as pinholes in transport layers. As illustrated in Fig. 5, photoinduced excess holes at the valence band edges can attack the Au contact, lowering both the formation energy of Au_i^+ and the threshold voltage for Au oxidation photoelectrochemically. This effect can be more pronounced in n–i–p devices where the anodic bias at the top Au electrode during operation can drive Au oxidation and migration purely electrochemically. Moreover, reverse bias conditions due to partial shading in a p–i–n sub-cell within a module can impose a strong anodic potential on the Au contact, promoting rapid Au migration through pinholes and leading to the formation of metallic shunts and

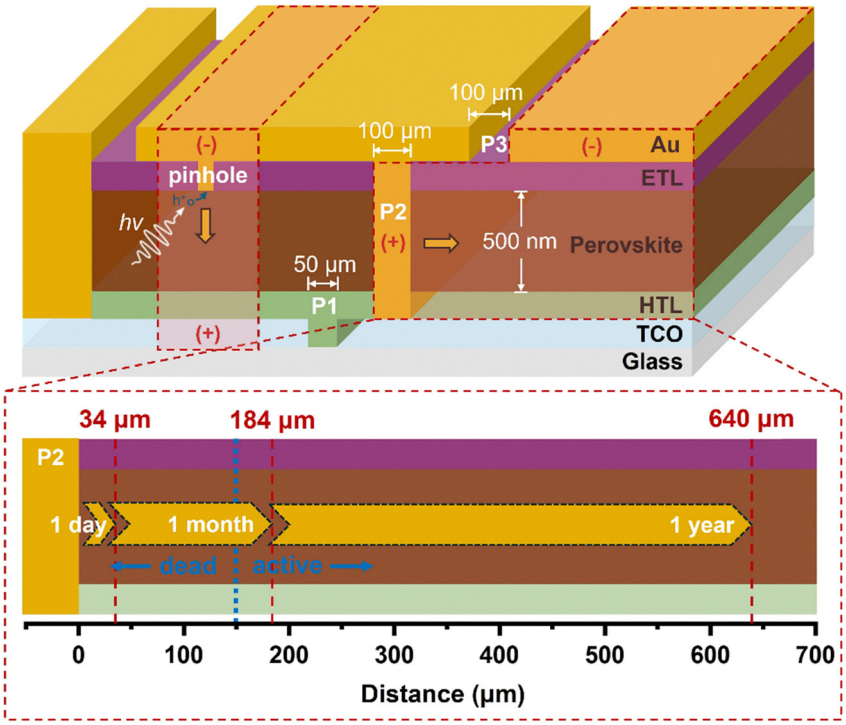

Fig. 5 Schematic illustration of two adjacent active cells connected in series in a monolithically integrated perovskite PV module separated by the P1, P2, and P3 scribes. Typical perovskite layer thickness and representative scribe widths are indicated. Two possible pathways for Au migration are highlighted in red. The bottom panel shows the estimated diffusion lengths ($L = (Dt)^{1/2}$) after 1 day, 1 month, and 1 year of operation, based on the experimentally extracted Au_i^+ diffusion coefficient. The approximate boundary between the dead and active areas near the P2 scribe is marked by a blue dashed line for reference.

localized hot-spots.[56] Photochemistry may also play a role in n–i–p devices by release of iodine that can then travel through the organic HTL to directly attack the Au.[20]

Another critical pathway exists at the direct perovskite/Au interface along the P2 scribes in p–i–n modules, where, under normal operational conditions, the Au contact is nominally biased anodically relative to the Au electrode of the adjacent sub-cell separated by the P3 scribe (Fig. 5). In other words, *the Au/perovskite interface experiences an oxidative driving force due to the layout of a thin film module*. This provides the possibility to dissolve a significant amount of Au where long times and lateral migration enables long-range distribution of Au species within the perovskite layer. Based on our extracted Au_i^+ diffusion coefficient ($D = 1.3 \times 10^{-10}$ cm^2 s^{-1}), the estimated Au diffusion lengths ($L \sim [Dt]^{1/2}$) are approximately 34 μm, 184 μm, and 640 μm after 1 day, 1 month, and 1 year, respectively. Note these are underestimated since solar cells and PV modules typically rise well above room temperature. Considering that P3 scribes are typically ~100 μm wide,[57] substantial Au species could diffuse into the active area within a month of operation, potentially compromising long-term PV performance. This issue may arise sooner and more severely as the field continues to reduce P3 scribe widths to improve module efficiency.

Above, we described photoelectrochemical oxidation of Au by photogenerated holes. To fully understand the reactivity, one also needs to consider photoelectrochemical reduction of Au_i^+ by conduction band electrons. This reaction would be capable of reducing Au_i^+ within the bulk or at grain boundaries forming small Au^0 colloids, which would almost certainly act as recombination sites. We believe reduction by conduction band electrons can also occur in the dark when driving at suprathreshold voltages as we have observed previously.[20] Per Fig. 5i–l, electron conduction will be significant at higher voltages and long times. These considerations barely scratch the surface of the complex interplay between photochemical, photoelectrochemical, and electrochemical reactions that must be analyzed on a case-by-case basis given the sample/device architecture and experimental conditions.

In general, these results inform a more comprehensive understanding of Au migration characteristics in halide perovskite devices, highlighting both its low thermodynamic threshold and rapid transport kinetics despite relatively low diffusion coefficients. We provide the first robust estimations for D and C_0 for Au_i^+ based on solid experimental data which allows the calculation of ion transport kinetics in real systems and informs the foundation for future drift-diffusion modelling. These insights underscore the close correlation between extrinsic metal ion redistribution and the electrical response of the device, thus shedding light on the potential origins of device instabilities in perovskite-based solar cells and LEDs, while also suggesting possible operating mechanisms of perovskite-based memory devices and switchable photovoltaics.[17,21,23] Moreover, this study further demonstrates the added nature of perovskite devices as solid-state electrochemical cells and

exemplifies the utility of semi-quantitative modelling/analysis in probing ion migration within this electrolytic system.

Conclusion

This work comprehensively investigated the kinetics and dynamics of Au^+ ion migration in $MAPbI_3$ perovskite devices under potentiostatic bias. We demonstrate that Au^+ cations migrate rapidly through the perovskite lattice, initiating at the Au anode and precipitating at the ITO cathode as Au^0 islands, profoundly influencing device electrical behavior through electrochemical doping and interfacial barrier modulation. The Au^+ migration kinetics can be modulated by perovskite stoichiometry, with MAI-deficient films exhibiting faster transport. Through temporal and spatial characterization, we determine diffusion coefficients on the order of 10^{-11} to 10^{-10} cm^2 s^{-1}, demonstrating a semi-quantitative experimental approach to study extrinsic metal ion migration kinetics within halide perovskites. Additionally, we show that Au plating is partially reversible through reversing bias polarity, drawing a compelling parallel to Li plating/stripping in solid-state batteries. These findings highlight perovskite devices as solid-state electrochemical systems where ionic and electronic processes are intricately coupled. The results suggest further mechanistic insight into the origins of device instability and anomalous behavior in perovskite photovoltaics or LEDs, emphasizing the direct impact of extrinsic metal redistribution. Moreover, they offer opportunities for functional device applications, such as perovskite-based memristors or switchable devices enabled by voltage-controlled metal ion migration.

Conflicts of interest

There are no conflicts to declare.

Data availability

The data supporting this article have been included as part of the supplementary information (SI). Supplementary information is available. See DOI: **https://doi.org/10.1039/d5ee04569j**.

Acknowledgements

B. P. R., T. H., and Q. X. acknowledge support for this work by the Department of the Navy, Office of Naval Research under ONR award no. N00014-23-1-2021. This work was authored in part by the National Renewable Energy Laboratory for the U.S. Department of Energy (DOE) under Contract No. DE-AC36-08GO28308. Funding for R. A. K. provided by the ''Perovskite Enabled Tandems'' project funded by the US Department of Energy Office of Energy Efficiency and Renewable Energy (EERE **https://ror.org/02xznz413**) and Solar Energy Technologies Office (SETO **https://ror.org/033jmdj81**) under Award #52776. The views expressed in the article do not necessarily represent the views of the DOE or the U.S. Government. The U.S. Government retains and the publisher, by accepting the article for publication, acknowledges that the U.S. Government retains a non-exclusive, paid-up, irrevocable, worldwide license to publish or reproduce the published form of this work, or allow others to do so, for U.S. Government purposes. R. A. K. thanks Drs. Axel F. Palmstrom and Joseph J. Berry for productive discussions. A. K. and Y. R. acknowledge support by the Eric and Wendy Schmidt Transformative Technology Fund. L. K. thanks the Minerva Centre for Self-Repairing Systems for Energy & Sustainability, the Mintzi and Aryeh Katzman Professorial Chair, and the Helen and Martin Kimmel Award for Innovative Investigation, for their support.

References

1 A. Kojima, K. Teshima, Y. Shirai and T. Miyasaka, *J. Am. Chem. Soc.*, 2009, **131**, 6050–6051.
2 M. M. Lee, J. Teuscher, T. Miyasaka, T. N. Murakami and H. J. Snaith, *Science*, 2012, **338**, 643–647.
3 M. A. Green, A. Ho-Baillie and H. J. Snaith, *Nat. Photonics*, 2014, **8**, 506–514.
4 National Renewable Energy Laboratory, Best Research-Cell Efficiency Chart, **https://www.nrel.gov/pv/cell-efficiency.html**, accessed June 6, 2025.
5 Z.-K. Tan, R. S. Moghaddam, M. L. Lai, P. Docampo, R. Higler, F. Deschler, M. Price, A. Sadhanala, L. M. Pazos, D. Credgington, F. Hanusch, T. Bein, H. J. Snaith and R. H. Friend, *Nat. Nanotechnol.*, 2014, **9**, 687–692.
6 Z. Xiao, R. A. Kerner, L. Zhao, N. L. Tran, K. L. Lee, T. W. Koh, G. D. Scholes and B. P. Rand, *Nat. Photonics*, 2017, **11**, 108–115.
7 A. Fakharuddin, M. K. Gangishetty, M. Abdi-Jalebi, S. H. Chin, A. R. bin Mohd Yusoff, D. N. Congreve, W. Tress, F. Deschler, M. Vasilopoulou and H. J. Bolink, *Nat. Electron.*, 2022, **5**, 203–216.
8 H. Tian, L. Zhao, X. Wang, Y. W. Yeh, N. Yao, B. P. Rand and T. L. Ren, *ACS Nano*, 2017, **11**, 12247–12256.
9 X. Xiao, J. Hu, S. Tang, K. Yan, B. Gao, H. Chen and D. Zou, *Adv. Mater. Technol.*, 2020, **5**, 1900914.
10 R. A. John, N. Shah, S. K. Vishwanath, S. E. Ng, B. Febriansyah, M. Jagadeeswararao, C. H. Chang, A. Basu and N. Mathews, *Nat. Commun.*, 2021, **12**, 3681.
11 C. Eames, J. M. Frost, P. R. F. Barnes, B. C. O'Regan, A. Walsh and M. S. Islam, *Nat. Commun.*, 2015, **6**, 7497.
12 D. A. Egger, A. M. Rappe and L. Kronik, *Acc. Chem. Res.*, 2016, **49**, 573–581.
13 J. M. Frost and A. Walsh, *Acc. Chem. Res.*, 2016, **49**, 528–535.
14 Z. Xu, R. A. Kerner, L. Kronik and B. P. Rand, *ACS Energy Lett.*, 2024, **9**, 4645–4654.
15 H. J. Snaith, A. Abate, J. M. Ball, G. E. Eperon, T. Leijtens, N. K. Noel, S. D. Stranks, J. T. W. Wang, K. Wojciechowski and W. Zhang, *J. Phys. Chem. Lett.*, 2014, **5**, 1511–1515.
16 W. Tress, N. Marinova, T. Moehl, S. M. Zakeeruddin, M. K. Nazeeruddin and M. Gratzel, *Energy Environ. Sci.*, 2015, **8**, 995–1004.

17 Z. Xiao, Y. Yuan, Y. Shao, Q. Wang, Q. Dong, C. Bi, P. Sharma, A. Gruverman and J. Huang, *Nat. Mater.*, 2015, **14**, 193–198.
18 Y. Yuan, J. Chae, Y. Shao, Q. Wang, Z. Xiao, A. Centrone and J. Huang, *Adv. Energy Mater.*, 2015, **5**, 1500615.
19 L. Zhao, R. A. Kerner, Z. Xiao, Y. H. L. Lin, K. M. Lee, J. Schwartz and B. P. Rand, *ACS Energy Lett.*, 2016, **1**, 595–602.
20 R. A. Kerner, L. Zhao, S. P. Harvey, J. J. Berry, J. Schwartz and B. P. Rand, *ACS Energy Lett.*, 2020, **5**, 3352–3356.
21 R. A. Kerner, A. V. Cohen, Z. Xu, A. R. Kirmani, S. Y. Park, S. P. Harvey, J. P. Murphy, R. C. Cawthorn, N. C. Giebink, J. M. Luther, K. Zhu, J. J. Berry, L. Kronik and B. P. Rand, *Adv. Mater.*, 2023, **35**, 2302206.
22 Y. Zhang, A. Ummadisingu, R. Shivanna, D. H. L. Tjhe, H. I. Un, M. Xiao, R. H. Friend, S. P. Senanayak and H. Sirringhaus, *Small*, 2023, **19**, 2302494.
23 P. Liu, T. Dai, C. Yan, G. Bai, S. Lu, Z. Wang, Z. Lou, Y. Hou, F. Teng and Y. Hu, *J. Phys. Chem. Lett.*, 2025, **16**, 4480–4488.
24 Y. Kato, L. K. Ono, M. V. Lee, S. Wang, S. R. Raga and Y. Qi, *Adv. Mater. Interfaces*, 2015, **2**, 1500195.
25 J. Wang, S. P. Senanayak, J. Liu, Y. Hu, Y. Shi, Z. Li, C. Zhang, B. Yang, L. Jinag, D. Di, A. V. Ievlev, O. S. Ovchinnikova, T. Ding, H. Deng, L. Tang, Y. Guo, J. Wang, K. Xiao, D. Venkateshvaran, L. Jiang, D. Zhu and H. Sirringhaus, *Adv. Mater.*, 2019, **31**, 1902618.
26 S. Svanström, T. J. Jacobsson, G. Boschloo, E. M. J. Johansson, H. Rensmo and U. B. Cappel, *ACS Appl. Mater. Interfaces*, 2020, **12**, 7212–7221.
27 R. A. Kerner, P. Schulz, J. A. Christians, S. P. Dunfield, B. Dou, L. Zhao, G. Teeter, J. J. Berry and B. P. Rand, *APL Mater.*, 2019, **7**, 041113.
28 K. Domanski, J. P. Correa-Baena, N. Mine, M. K. Nazeeruddin, A. Abate, M. Saliba, W. Tress, A. Hagfeldt and M. Gratzel, *ACS Nano*, 2016, **10**, 6306–6314.
29 C. Besleaga, L. E. Valentin, V. Stancu, A. G. Tomulescu, M. Sima, L. Trinca, N. Plugaru, L. Pintilie, G. A. Nemnes, M. Iliescu, H. G. Svavarsson, A. Manolescu and I. Pintilie, *J. Phys. Chem. Lett.*, 2016, **7**, 5168–5175.
30 Z. Xu, R. A. Kerner, S. P. Harvey, K. Zhu, J. J. Berry and B. P. Rand, *ACS Energy Lett.*, 2022, **8**, 513–520.
31 R. A. Z. Razera, D. A. Jacobs, F. Fu, P. Fiala, M. Dussouillez, F. Sahli, T. C. J. Yang, L. Ding, A. Walter, A. F. Feil, H. I. Boudinov, S. Nicolay, C. Ballif and Q. Jeangros, *J. Mater. Chem. A*, 2020, **8**, 242–250.
32 C. Ding, L. Yin, L. Zhang, R. Huang, S. Fan, Q. Luo, J. Lin, F. Li, C. Zhao, R. Osterbacka and C. Q. Ma, *Adv. Funct. Mater.*, 2021, **31**, 2103820.
33 J. C. Pérez-Martínez, M. Berruet, C. Gonzales, S. Salehpour, A. Bahari, B. Arredondo and A. Guerrero, *Adv. Funct. Mater.*, 2023, **33**, 2305211.
34 I. H. Im, S. J. Kim, J. H. Baek, K. J. Kwak, T. H. Lee, J. W. Yang, D. E. Lee, J. Y. Kim, H. R. Kwon, D. Y. Heo, S. Y. Kim and H. W. Jang, *Adv. Funct. Mater.*, 2023, **33**, 2211358.
35 I. H. Im, J. H. Baek, S. J. Kim, J. Kim, S. H. Park, J. Y. Kim, J. J. Yang and H. W. Jang, *Adv. Mater.*, 2024, **36**, 2307334.
36 D. Cao, X. Sun, Q. Li, A. Natan, P. Xiang and H. Zhu, *Matter*, 2020, **3**, 57–94.
37 Z. Ning, G. Li, D. L. Melvin, Y. Chen, J. Bu, D. Spencer-Jolly, J. Liu, B. Hu, X. Gao, J. Perera and C. Gong, *Nature*, 2023, **618**, 287–293.
38 A. Watt and A. Philip, *Electroplating and Electrorefining of Metals*, Watchmaker Publishing, 2005.
39 R. A. Kerner and B. P. Rand, *ACS Appl. Energy Mater.*, 2019, **2**, 6097–6101.
40 L. Zhao, K. Roh, S. Kacmoli, K. Al Kurdi, S. Jhulki, S. Barlow, S. R. Marder, C. Gmachl and B. P. Rand, *Adv. Mater.*, 2020, **32**, 2000752.
41 Y. Jiang, S. C. Yang, Q. Jeangros, S. Pisoni, T. Moser, S. Buecheler, A. N. Tiwari and F. Fu, *Joule*, 2020, **4**, 1087–1103.
42 W. Ming, D. Yang, T. Li, L. Zhang and M. H. Du, *Adv. Sci.*, 2018, **5**, 1700662.
43 L. K. Ono, S. Liu and Y. Qi, *Angew. Chem., Int. Ed.*, 2020, **17**, 6676–6698.
44 J. Siekmann, S. Ravishankar and T. Kirchartz, *ACS Energy Lett.*, 2021, **6**, 3244–3251.
45 M. De Keersmaecker, N. R. Armstrong and E. L. Ratcliff, *Energy Environ. Sci.*, 2021, **14**, 4840–4846.
46 S. Bitton and N. Tessler, *Energy Environ. Sci.*, 2023, **16**, 2621–2628.
47 M. H. Futscher, J. M. Lee, L. McGovern, L. A. Muscarella, T. Wang, M. I. Haider, A. Fakharuddin, L. Schmidt-Mende and B. Ehrler, *Mater. Horiz.*, 2019, **6**, 1497–1503.
48 A. Senocrate, I. Moudrakovski, G. Y. Kim, T. Y. Yang, G. Gregori, M. Gratzel and J. Maier, *Angew. Chem., Int. Ed.*, 2017, **56**, 7755–7759.
49 C. Eames, J. M. Frost, P. R. F. Barnes, B. C. O'Regan, A. Walsh and M. S. Islam, *Nat. Commun.*, 2015, **6**, 7497.
50 C. Li, A. Guerrero, S. Huettner and J. Bisquert, *Nat. Commun.*, 2018, **9**, 5513.
51 Y. Liang, F. Li, X. Cui, C. Stampfl, S. P. Ringer, X. Yang, J. Huang and R. Zheng, *Sci. Adv.*, 2025, **11**, 7054.
52 Y. Lu, C. Z. Zhao, J. K. Hu, S. Sun, H. Yuan, Z. H. Fu, X. Chen, J. Q. Huang, M. Ouyang and Q. Zhang, *Sci. Adv.*, 2022, **8**, eadd0510.
53 T. Schmaltz, F. Hartmann, T. Wicke, L. Weymann, C. Neef and J. Janek, *Adv. Energy Mater.*, 2023, **13**, 2301886.
54 A. Manthiram, X. Yu and S. Wang, *Nat. Rev. Mater.*, 2017, **2**, 16103.
55 F. Zhang, F. Ullrich, S. Silver, R. A. Kerner, B. P. Rand and A. Kahn, *J. Phys. Chem. Lett.*, 2019, **10**, 890–896.
56 A. R. Bowring, L. Bertoluzzi, B. C. O'Regan and M. D. McGehee, *Adv. Mater.*, 2018, **8**, 1702365.
57 J. Zhang, X. Ji, X. Wang, L. Zhang, L. Bi, Z. Su, X. Gao, W. Zhang, L. Shi, G. Guan, A. Abudula, X. Hao, L. Yang, Q. Fu, A. K.-Y. Jen and L. Lu, *Nano-Micro Lett.*, 2024, **16**, 190.